JOURNAL OF THERMOPHYSICS AND HEAT TRANSFER
Vol. 19, No. 2, April–June 2005

Modeling the Floating Zone: Instabilities in the Half Zone and Full Zone

B. C. Houchens* and J. S. Walker†
University of Illinois, Urbana–Champaign, Urbana, Illinois 61801

Linear stability analyses are performed on steady, axisymmetric base flows in a laterally heated floating zone (full zone) in microgravity. We treat fully three-dimensional disturbances for a range of Prandtl numbers less than 0.2 and aspect ratios (total zone height to diameter) varying from $\frac{1}{2}$ to 2. In all cases, the critical mode is a transition to a steady three-dimensional flow. Axial symmetry of the disturbance, and the critical wave number, vary with both Prandtl number and aspect ratio. Results are compared and contrasted to the linear stability of the half-zone model, which is commonly used to approximate one-half of the full zone. Findings indicate that the stability analysis of the half zone is a reasonable approximation to that of the full zone for Prandtl numbers less than approximately 0.05, in zones with aspect ratios near unity. The dominant mechanism for feeding energy into the perturbation, as well as the critical wave number, is the same in both models. However, the driving force required for the onset of instability in the half zone is 25–50% larger than that in the full zone. As the Prandtl number is increased, the two models become more divergent, first with respect to the predicted critical values, and then in the instability mechanisms themselves.

Introduction

IN the floating-zone process, a body of molten semiconductor is held by surface tension between the melting end of a cylindrical feed rod and the solidifying end of a colinear cylindrical single crystal. There are two advantages of the floating-zone process. First, there is no contamination from melt contact with an ampoule or crucible. Second, defects incurred by differential contraction (during the cooling of crystals grown inside ampoules) are eliminated. In the ellipsoidal furnace developed by Eyer et al.[1] for floating-zone crystal growth in space, the radiation from an optical source at one focal point provides the heat flux needed to produce and maintain the melt region as the feed rod is moved through the other focal point. These authors present several experimental schematics of various furnace configurations. The simplified model is sketched in Fig. 1. There is an axisymmetric heat flux into the essentially cylindrical free surface, so that the temperature of the free surface varies from a maximum at the middle of the circumference to the solidification temperature at the peripheries of both the feed rod and the crystal. Because the surface tension of most molten semiconductors decreases as the temperature is increased, surface-tension variations drive two toroidal melt circulations with flows along the free surface from the hottest circumference toward both the feed rod and crystal, and with the return flows near the centerline.[2] Instabilities in this thermocapillary convection often lead to periodic nonaxisymmetric melt motion. Associated fluctuations in the mass transport of additives or dopants leads to undesirable spatial oscillations of the dopant concentration in the crystal, which are called striations.[3] Clearly a thorough understanding of the thermocapillary instability is needed in order to grow striation-free crystals with the floating-zone process.

Most previous studies of the thermocapillary instability for a finite-length cylindrical free surface have used the half-zone (HZ) model. In the HZ model, there is a cylindrical, thermally insulated free surface between two planar solid disks at different temperatures. The HZ model is assumed to approximate half of the actual floating-zone process, with the hotter disk representing the plane of the hottest circumference and the colder disk representing either the crystal–melt or the feed rod–melt interface. The present paper presents a linear stability analysis for a more realistic representation of the actual floating-zone process, which we call the full-zone (FZ) model. In our FZ model, there is a parabolic heat flux into the cylindrical free surface, and the temperature is the same at the two planar liquid–solid interfaces. A primary purpose of the present paper is to compare predictions from the HZ and FZ models. A key parameter is the ratio of the axial height of the cylindrical liquid zone to its diameter, or the aspect ratio b. The aspect ratio for the HZ model is one-half of that for the comparable FZ.

Wanschura et al.[4] presented a linear stability analysis for nonaxisymmetric perturbations to the HZ. They showed that the first instability involves a transition to a nonaxisymmetric steady flow for small values of the Prandtl number Pr and a transition to a nonaxisymmetric periodic flow for large Pr. There was a range of Pr between these two instabilities for which they could not obtain numerically accurate results. Houchens and Walker[5] verified the mode identified by Wanshura et al. for $Pr = 0.02$ and investigated the effects of applying a uniform axial magnetic field to damp this instability. Chen et al.[6] presented a thorough linear stability analysis for the HZ model over a range of Pr from 10^{-10} to 8 and were able to reduce the gap in Pr where numerically accurate results could not be obtained. Many of the results of Chen et al.[6] are used here for comparison to the FZ results. The gap in Pr was recently bridged by Levenstam et al.[7] using both linear stability analyses and time integrations of the full nonlinear three-dimensional equations. The results in these four papers[4–7] using the HZ model agree well except in the range $0.05 < Pr < 0.8$. The results for larger values of Pr, namely 1 and 4, have been confirmed by Sim and Zebib,[8] who also looked at the effect of a curved free surface. Wanschura et al.[4] also treated axisymmetric perturbations, which were never critical, so that the entire range of azimuthal wave number possibilities has been covered for a wide range of Pr for the HZ problem.

Kasperski et al.[9] presented a linear stability analysis for axisymmetric perturbations for the FZ model with a polynomial variation of the heat flux into the cylindrical free surface. They showed that axisymmetric perturbations are stable up to very large values of the Reynolds number Re, based on thermocapillary convection. Mortland and Walker[10] presented time integrations of the axisymmetric equations for the FZ model with a strong axial magnetic field. They

Presented as Paper 2003-1313 at the 41st Aerospace Sciences Meeting and Exhibit, Reno, NV, 6 January 2003; received 30 April 2003; revision received 9 July 2004; accepted for publication 12 July 2004.

*Postdoctoral Research Associate, Department of Mechanical and Industrial Engineering, MC-244. Member AIAA.

†Professor, Department of Mechanical and Industrial Engineering, MC-244.

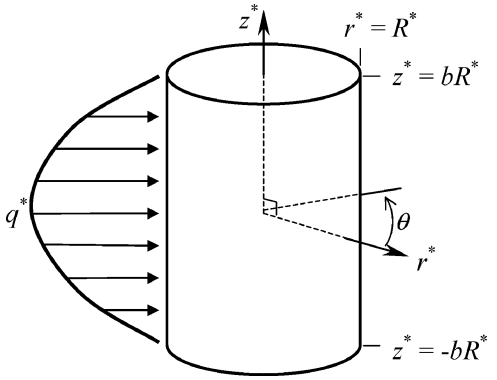

Fig. 1 FZ geometry with parabolic heat flux.

did not find any transitions from the steady base flow for the values of Re for which numerically accurate results could be obtained.

To our knowledge, there has been no previous linear stability analysis for nonaxisymmetric perturbations for the FZ model, though Lappa[11] studied a similar full-zone model using three-dimensional time integrations for $Pr = 0.01$. Comparisons to this work are included when possible. Here we present results for ranges of Pr and b, which are typical of the floating-zone growth of various semiconductor crystals. The purpose of this paper is twofold. First, we give a strong justification for the enormous amount of time spent on studies of the half zone. This model has, only recently, approached the classification of a well-understood problem. We show that indeed, for many of the materials of interest, the half zone is able to capture the qualitative physics of floating-zone crystal growth. The second purpose is to begin moving toward more realistic models. These will allow new materials, which are of great value but often fastidious about their handling, to be processed using specifically tailored, floating-zone crystal growth methods.

Problem Formulation

A model of a full floating zone typical of those used for growing radiatively heated semiconductor crystals is shown in Fig. 1. The heat flux into the melt in the radial direction is assumed to vary parabolically so that

$$k^* \frac{\partial T^*}{\partial r^*} = q^* \left[1 - \left(\frac{z^*}{bR^*} \right)^2 \right] \tag{1}$$

where k^* is the thermal conductivity of the melt, T^* is the dimensional temperature, q^* is the maximum value of the heat flux, b is the aspect ratio, R^* is the radius of the cylindrical melt region, and r^* and z^* are the dimensional cylindrical coordinates. The temperature variation along the free surface results in a gradient in surface tension. Near the axial midplane ($z^* = 0$), the free surface is hottest and the surface tension is smallest. At the cooler ends of the melt, the surface tension is greatest. This potential drives a set of axisymmetric toroidal thermocapillary convection cells. The surface tension is assumed to be a linearly decreasing function of temperature given by

$$\gamma^*(T^*) = \gamma_o^* + \frac{\mathrm{d}\gamma^*}{\mathrm{d}T^*}\left(T^* - T_s^*\right) \tag{2}$$

where $\mathrm{d}\gamma^*/\mathrm{d}T^*$ is a negative quantity. The reference surface tension γ_o^* is assumed to be large enough that the free surface remains cylindrical. In microgravity, the actual free-surface shape is slightly bulged near $z^* = 0$ and is referred to as the barrel shape.[12] This small modification to the flow geometry is neglected here.

A schematic of the HZ model to which comparisons are made can be found in Levenstam et al.[7] The HZ geometry is intended to model the FZ (Fig. 1) from the region of maximum heat flux to the top solidification boundary. Axial heat flux is modeled in the HZ by making the bottom boundary hot, the top the melting temperature, and the free surface insulating, producing a temperature gradient on the free surface. Treatment of the stability of the HZ with a deformable free surface can be found in Sim and Zebib[8] and Nienhüser and Kuhlmann.[13]

The FZ nondimensionalization is the same as that used by Prange et al.[14] in their study of the HZ. A viscous scale is chosen for the characteristic velocity such that $V^* = \mu^*/(\rho^* R^*)$, where μ^* is the absolute viscosity and ρ^* is the density of the melt. The scales for length, time, and pressure are R^*, R^{*2}/ν^*, and $\rho^* \nu^{*2}/R^{*2}$, respectively, where ν^* is the kinematic viscosity, defined as $\nu^* \equiv \mu^*/\rho^*$. The characteristic temperature difference is $\Delta T_{\mathrm{FZ}}^* = q^* R^*/k^*$. The temperature is nondimensionalized by subtracting the solidification temperature T_s^* and dividing by ΔT_{FZ}^*. The dimensionless parameters that appear in the governing equations and boundary conditions are

$$Pr = \frac{\mu^* c_p^*}{k^*} \tag{3a}$$

$$Re_{\mathrm{FZ}} = \rho^* R^* \left| \frac{\mathrm{d}\gamma^*}{\mathrm{d}T^*} \right| \Delta T_{\mathrm{FZ}}^* \Big/ \mu^{*2} \tag{3b}$$

where c_p^* is the specific heat of the melt. These parameters are the Prandtl and Reynolds numbers, respectively. The Prandtl number is a material property. Materials with Pr in the range studied here include indium-phosphide ($Pr_{\mathrm{In-P}} \approx 0.015$; see Ref. 15), silicon ($Pr_{\mathrm{Si}} \approx 0.02$), and gallium–arsenide ($Pr_{\mathrm{Ga-As}} \approx 0.068$; see Ref. 15). The Reynolds number is a measure of the driving potential of the temperature and surface-tension gradients that produce the thermocapillary flow.

The nondimensional governing equations are incompressible continuity, the Navier–Stokes equations, and the energy equation, neglecting viscous dissipation:

$$\nabla \cdot v = 0 \tag{4a}$$

$$\frac{\partial v}{\partial t} + (v \cdot \nabla) v = -\nabla P + \nabla^2 v \tag{4b}$$

$$Pr\left[\frac{\partial T}{\partial t} + (v \cdot \nabla) T \right] = \nabla^2 T \tag{4c}$$

The boundary conditions are

$$v_r = 0 \tag{5a}$$

$$\frac{\partial}{\partial r}\left(\frac{v_\theta}{r} \right) = -Re_{\mathrm{FZ}} \frac{\partial T}{\partial \theta} \tag{5b}$$

$$\frac{\partial v_z}{\partial r} = -Re_{\mathrm{FZ}} \frac{\partial T}{\partial z} \tag{5c}$$

$$\frac{\partial T}{\partial r} = 1 - \left(\frac{z}{b} \right)^2, \qquad \text{at} \qquad r = 1 \tag{5d}$$

$$v_r = 0 \tag{5e}$$

$$v_\theta = 0 \tag{5f}$$

$$v_z = 0 \tag{5g}$$

$$T = 0, \qquad \text{at} \qquad z = \pm b \tag{5h}$$

The subscripts FZ in (3b) indicate that this is the appropriate Reynolds number for the full-zone analysis, with a characteristic temperature difference proportional to the maximum value of the heat flux. This makes comparison to the half zone somewhat awkward, because the half zone is scaled with a characteristic temperature difference $\Delta T_{\mathrm{HZ}}^* = T_{\mathrm{hot}}^* - T_s^*$, where T_{hot}^* is the fixed, uniform dimensional temperature of the bottom wall. The resulting nondimensional temperatures on the top and bottom walls of the HZ are 0 and 1, respectively (or $-\frac{1}{2}$ and $+\frac{1}{2}$), and the Reynolds number, Re_{HZ}, is given by Eq. (3b) with ΔT_{FZ}^* replaced by ΔT_{HZ}^*. In the FZ,

the top wall is fixed at T_s^*, but the axial midplane has a variable temperature across its radius. To achieve the best comparison between the two models, we can set the maximum dimensional temperature of the FZ at $r=1, z=0$ to T_{hot}^*. This allows us to relate the two Reynolds numbers with $Re_{\text{HZ}} = T_{\text{FZ,max}} Re_{\text{FZ}}$, where $T_{\text{FZ,max}}$ is the maximum dimensionless base-flow temperature from the FZ analysis (at $r=1, z=0$). Experimentally, this would amount to measuring the temperature at the middle of the free surface of a FZ and using this temperature as an input for specifying that of the bottom wall of a HZ, with the top wall held at T_s^*. Then, as the heat flux was increased in the FZ, the increase in maximum temperature at the free surface would be measured, and the temperature of the lower wall in the HZ would be increased accordingly. When comparing the two models, we will use the corrected $T_{\text{FZ,max}} Re_{\text{FZ}}$ values. Otherwise, we will use Re_{FZ} because it is a stretched scale that allows better benchmarking of the FZ results.

Base Flow

The steady, axisymmetric base flow, with zero azimuthal velocity, is solved as described by Houchens and Walker,[5] using a fourth-order stream function–temperature formulation. The equation governing the stream function is really a conservation statement on the azimuthal vorticity (which is the only nonzero component). When this component of vorticity is written in terms of velocity gradients, and the velocities are replaced by the stream function, the vorticity-transport equation becomes a fourth-order biharmonic-type equation governing the stream function. The base-flow stream function Ψ and temperature T_0 are expanded in the product of their radial and axial Chebyshev polynomial series representations, with appropriate factors of r that correspond to their behavior near $r=0$ ($\Psi \sim r^2$, and $T_0 \sim r^0$). Taking advantage of the symmetry in the boundary conditions and the geometry, the unique solution domain is $0 \le r \le 1$ and $0 \le z \le b$. Because the symmetry in the radial direction is accounted for by the power of r multiplying each series, only the even radial Chebyshev polynomials are used in the representations, ensuring that the correct radial symmetry is maintained. Appropriate symmetry in the axial direction is achieved by using the odd polynomials for Ψ and the even polynomials for T_0. With the radial and axial Chebyshev polynomials defined as $T_L(r)$ and $T_N(z/b)$, respectively, the expansions for Ψ and T_0 are

$$\Psi\left(r, \frac{z}{b}\right) = r^2 \sum_{L=0}^{\text{NRF}+1} \sum_{N=0}^{\text{NZF}+1} A_{LN} T_{2L}(r) T_{2N+1}\left(\frac{z}{b}\right) \quad (6a)$$

$$T_0\left(r, \frac{z}{b}\right) = \sum_{L=0}^{\text{NRT}} \sum_{N=0}^{\text{NZT}} B_{LN} T_{2L}(r) T_{2N}\left(\frac{z}{b}\right) \quad (6b)$$

where A_{LN} and B_{LN} are the sets of coefficients that must be found and NRF, NZF, NRT, NZT represent the number of collocation points. These expansions are applied to two Gauss–Lobatto collocation grids,

$$r_{I\xi} = \cos(I_\xi \pi / 2NR\xi) \quad \text{for} \quad I_\xi \text{ going 0 to } NR\xi \quad (7a)$$

$$z_{K\xi}/b = \cos(K_\xi \pi / 2NZ\xi) \quad \text{for} \quad K_\xi \text{ going 0 to } NZ\xi \quad (7b)$$

one for the stream function with ξ replaced by F, and one for the temperature field with ξ replaced by T, to coincide with the number of terms in the representations in (6a) and (6b), respectively. Two grids are used to take advantage of the fact that fewer terms are needed in the representation of T_0 than in that of Ψ, for small Pr. The regularization function, used to remove the discontinuity at the corner ($r=1, z=b$) between the thermocapillary boundary condition on the free surface and the no-slip condition on Ψ, is

$$F(z/b) = 1 - \exp\{-\alpha\,[1 - (z/b)^2]^2\} \quad (8)$$

As the positive regularization parameter α is increased, the limit of no regularization is approached. As a result of this smoothing, it is necessary to investigate both grid convergence and regularization-parameter convergence.

Because of the application of symmetry, the momentum equation governing Ψ is identically zero at both $r=0$ and $z=0$. Furthermore, because the Gauss–Lobatto grid is used, the majority of the collocation points are concentrated near $r=1$ and $z=b$. Although this is convenient for resolving the gradients in the corner, the sacrifice is that the deepest interior points are quite far from $r=0$ and $z=0$. Therefore, we expand the Chebyshev polynomial representation of the momentum equation about $r=0$ and $z=0$ and apply the first nonzero order of the expansion at $r=0$ and $z=0$ to enforce constraints on Ψ at these locations.

The base flow is then solved using the Newton–Raphson iterative technique. The lower-upper (LU) decomposition and back substitution are performed using the LAPACK routine DGESV.[16]

Linear Stability Analysis

The base flow is subjected to general three-dimensional disturbances of the form

$$\Phi(r, \theta, z, t) = \Phi_0(r, z) + \varepsilon\,\text{Real}[\exp(\lambda t + im\theta)\Phi_1(r, z)] \quad (9)$$

where Φ represents each of v_r, v_z, P, T or iv_θ, ε is of infinitesimal magnitude, and m is the real integer azimuthal wave number. Notice that, because $v_{\theta 0} \equiv 0$, the governing equations require a phase shift in the eigenfunction $v_{\theta 1}$ in order to obtain purely real equations. The generalized perturbation of (9) is introduced into the governing equations (4a–4c) and the boundary conditions (5a–5h), and terms that are satisfied identically by the base flow are dropped, whereas terms that are quadratic in ε are neglected. The remaining terms form the homogeneous eigenvalue problem governing the stability of the base flow to nonaxisymmetric disturbances for a set of parameters (Re_{FZ}, b, Pr, m). The associated eigenvalue $\lambda = \lambda_r + i\lambda_i$ determines the stability of the flow, where λ_r is the growth rate and λ_i is the frequency of the disturbance. For $\lambda_r < 0$, the base flow is steady and the perturbation will decay. For a given set (b, Pr, m), neutral stability is reached by increasing the thermocapillary Reynolds number to $Re_{\text{FZ,cr}}$, at which point the real part of the leading eigenvalue (or pair) crosses the $\lambda_r = 0$ axis.

The eigenvalue problem is solved as follows. The perturbation continuity equation is solved for $v_{\theta 1}$, which is then eliminated from the momentum equations, the no-slip condition, and the thermocapillary boundary condition. The θ–momentum equation is used to eliminate P_1 from the radial and axial momentum equations, leaving a pair of fourth-order momentum equations, the energy equation, and boundary conditions governing v_{r1}, v_{z1}, and T_1. The behavior of each of the perturbation variables as r goes to zero is again incorporated into the Chebyshev polynomial expansions in r and z. To first order, $v_{r1} \sim r^{m-1}$, whereas v_{z1} and $T_1 \sim r^m$.

The natural symmetry of the boundary conditions, geometry, and base flow causes the equations to even–odd decouple into two modes, for small perturbations.[17] The first, which maintains the axial symmetry of the base flow, will be referred to as the symmetric mode. In this mode, v_{r1}, $v_{\theta 1}$, P_1, and T_1 are even functions of z, and v_{z1} is an odd function of z. Thus, axial flow cannot cross from the top toroidal cell to the bottom, and the symmetric mode is therefore expected to be similar to disturbance modes that arise in the HZ. Notice, however, for symmetric modes, that $v_{\theta 1}$ need not be zero between the two cells. In contrast, in the HZ, $v_{\theta 1}$ is forced to satisfy a no-slip condition at this location. Therefore, the symmetric FZ mode is less constrained than any mode allowed in the HZ.

The antisymmetric mode breaks the axial symmetry of the base flow, and v_{z1} is an even function of z, whereas v_{r1}, $v_{\theta 1}$, P_1, and T_1 are odd. In this mode, information passes, by way of the vertical disturbance flow, between the two toroidal base-flow cells. Clearly this mode is also not allowed in the HZ model, where a no-penetration condition constrains the flow.

The minimum value of the critical Reynolds number will be the value associated with one of these two modes.[18] We then have the choice of treating the entire domain, and observing which disturbance symmetry arises naturally, or treating half of the axial domain, and investigating disturbances with each symmetry. Comparing these approaches shows that the first will require twice as many

grid points (because the domain is twice as large), and half of the coefficients in the representation will be identically zero. Alternatively, by analyzing the modes separately, we halve the domain and keep only nonzero coefficients in our representations. This improves the representation by a factor of 4, without accruing additional computational expense, and without loss of generality. The sacrifice is that two codes must be developed. However, as discussed by Grants and Gerbeth,[18] the improvement in accuracy far outweighs this significant, but manageable cost. They show that poor axial resolution causes their code to jump to the wrong perturbation mode, one that is supercritical to the initial instability. Therefore, we treat each mode separately and present results only over the domain $0 \le z \le b$, as the flow in the lower half of the domain can be inferred from the symmetry of the disturbance.

The Chebyshev polynomial series representations are

$$v_{r1}\left(r, \frac{z}{b}\right) = r^{m-1} \sum_{L=0}^{NR+1} \sum_{N=0}^{NZ} \mathbf{A}_{LN} T_{2L}(r) T_N\left(\frac{z}{b}\right) \quad (10a)$$

$$v_{z1}\left(r, \frac{z}{b}\right) = r^{m} \sum_{L=0}^{NR} \sum_{N=0}^{NZ+1} \mathbf{B}_{LN} T_{2L}(r) T_N\left(\frac{z}{b}\right) \quad (10b)$$

$$T_1\left(r, \frac{z}{b}\right) = r^{m} \sum_{L=0}^{NR} \sum_{N=0}^{NZ} \mathbf{C}_{LN} T_{2L}(r) T_N\left(\frac{z}{b}\right) \quad (10c)$$

where the axial polynomials are taken to satisfy the symmetry of each of the modes. The first nonzero term in the Taylor series of each of the governing equations is applied at $r = 0$ and $z = 0$, as described for the base flow. The vicinity of neutral stability is located using the EISPACK routine rgg.[19] Refinement and grid dependence studies are performed using the shifted inverse iteration method described by Saad (Chap. 4 in Ref. 20).

Energy Analysis

The contribution of terms that move energy from the base state to the perturbation is analyzed by returning to the time-dependent equations governing the evolutions of v_{r1}, $v_{\theta 1}$, v_{z1}, and T_1. The dot product of the perturbation velocity vector with the momentum equations gives energy evolution equations for v_{r1}^2, $v_{\theta 1}^2$, and v_{z1}^2. For v_{r1}^2 and v_{z1}^2 these have the form

$$\frac{1}{2}\frac{\partial\left(v_{r1}^2\right)}{\partial t} = -v_{r1}^2 \frac{\partial v_{r0}}{\partial r} - v_{r1} v_{z1} \frac{\partial v_{r0}}{\partial z} - \frac{1}{2}\left\{ v_{r0} \frac{\partial\left(v_{r1}^2\right)}{\partial r} + v_{z0} \frac{\partial\left(v_{r1}^2\right)}{\partial z} \right\}$$

$$- v_{r1} \frac{\partial P_1}{\partial r} + \text{diffusive terms} \quad (11a)$$

$$\frac{1}{2}\frac{\partial\left(v_{z1}^2\right)}{\partial t} = -v_{r1} v_{z1} \frac{\partial v_{z0}}{\partial r} - v_{z1}^2 \frac{\partial v_{z0}}{\partial z} - \frac{1}{2}\left\{ v_{r0} \frac{\partial\left(v_{z1}^2\right)}{\partial r} + v_{z0} \frac{\partial\left(v_{z1}^2\right)}{\partial z} \right\}$$

$$- v_{z1} \frac{\partial P_1}{\partial z} + \text{diffusive terms} \quad (11b)$$

The individual terms on the right-hand sides of (11a) and (11b) were computed at the critical point as functions of r and z.

Results and Discussion

The results section is divided up as follows. First, the primary instability mechanisms of the half zone and full zone are discussed for aspect ratio $b = 1$ with $Pr < 0.2$. The second section looks at the effects of varying the aspect ratio for fixed values of Pr. The mode switching associated with stretching and compressing the zone is discussed, and the results are compared to the corresponding half-zone data, as well as the full-zone study of Lappa.[11] The final section covers the numerical aspects of grid and regularization refinement and independence.

Varying the *Pr* for Aspect Ratio *b* = 1

The critical Re_{HZ} vs Pr is plotted for the FZ along with data for the HZ taken from Chen et al.[6] and Levenstam et al.[7] in Fig. 2 for $0 \le Pr \le 0.20$ and an aspect ratio $b = 1$. The FZ is most susceptible to disturbances with wave number $m_{\mathrm{cr}} = 2$, and all transitions are to a steady nonaxisymmetric flow. It should be noted that there is an antisymmetric $m = 1$ mode that becomes unstable at Re roughly 15% larger than the critical value, for $Pr < 0.05$, and results in a transition to periodic flow. Because the base flow is changed by the first instability, the linear stability analysis is not formally valid above $Re_{\mathrm{HZ,cr}}$. However, it does suggest that a second instability would occur shortly after the first and would likely involve a transition to periodic flow, as is typically observed experimentally. The maximum dimensionless temperature, $T_{\mathrm{FZ,max}}$, is plotted vs Pr for $b = 1$ in Fig. 3. The data for Figs. 2 and 3 are given in the Appendix.

Because $v_{\theta 1}$ goes as $-\sin(m_{\mathrm{cr}}\theta)$, the analysis of the perturbation variables can be confined to the quadrant wedge $0 \le \theta \le \pi/2$ for $m_{\mathrm{cr}} = 2$. No flow enters or leaves this quadrant, because $v_{\theta 1}$ is identically zero at both azimuthal boundaries. The perturbation variables v_{r1}, v_{z1}, and T_1 will always be plotted at $\theta = 0$, whereas $-v_{\theta 1}$ (which contributes positively to v_θ) will always be plotted at $\theta = \pi/4$. At these azimuthal planes, each perturbation variable has its maximum magnitude.

The presence of the second no-slip no-penetration surface in the HZ has a stabilizing effect that causes the model to overpredict the strength of flow needed for the onset of the first instability. For $Pr < 0.041$, the FZ has an antisymmetric critical mode. Over the range $0.041 < Pr < 0.079$, the critical mode is symmetric. For $0.079 < Pr \le 0.2$, discrepancies in the stability diagrams of the two

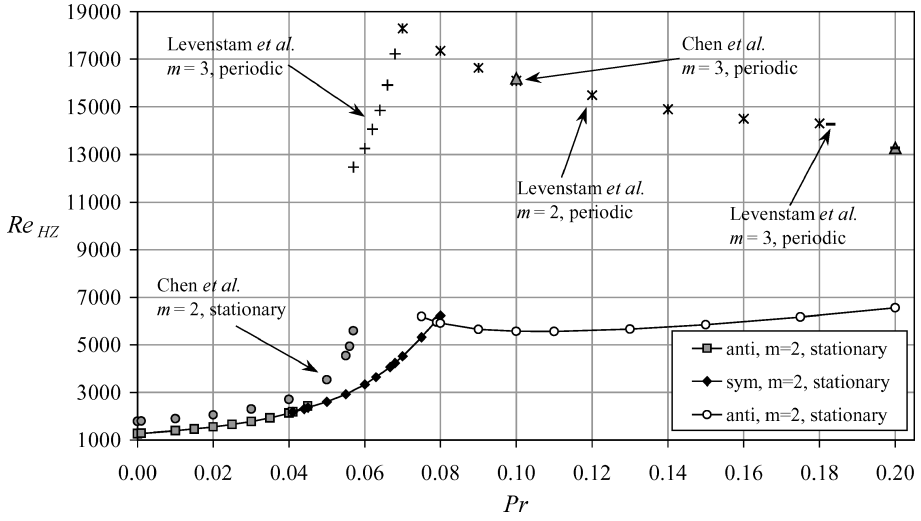

Fig. 2 $Re_{\mathrm{HZ,cr}}$ **vs** Pr **for the FZ with** $b = 1$**, and the corresponding HZ data taken from Chen et al.[6] and Levenstam et al.[7] Symbols connected by solid lines indicate the FZ data from this study with values given by** $T_{\mathrm{FZ,max}} Re_{\mathrm{FZ,cr}}$**.**

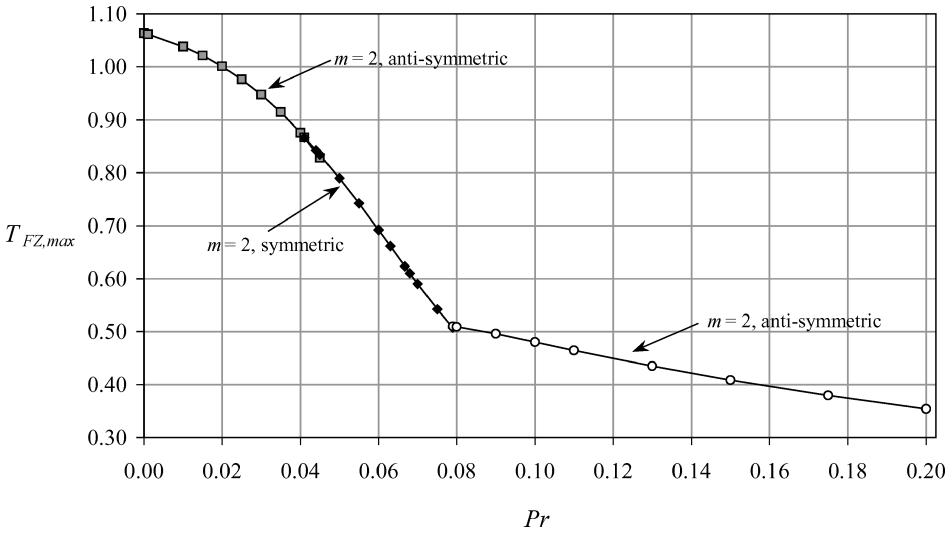

Fig. 3 $T_{FZ,max}$ vs Pr for the FZ with $b = 1$, at the transition to three-dimensional steady flow.

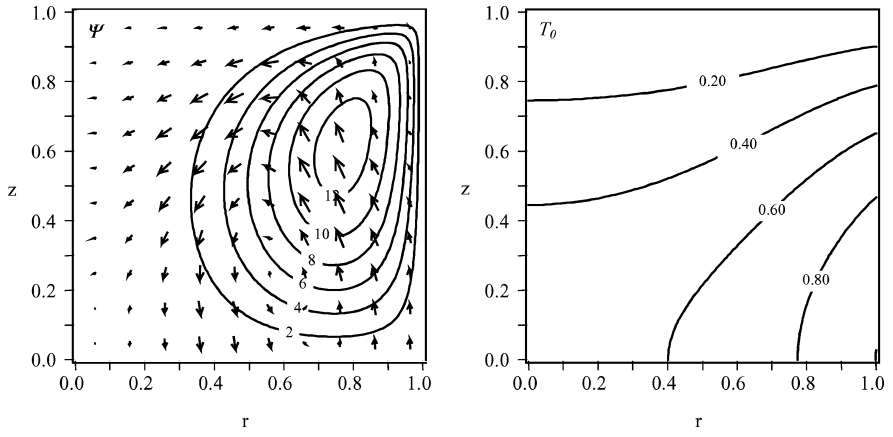

Fig. 4 Base-flow streamlines with perturbation velocity vectors defined by $v_{r1} + v_{z1}$ at $\theta = 0$, and isotherms for $Pr = 0.02$ at $Re_{FZ,cr} = 1546$ ($T_{FZ,max} = 1.0007$) for the $m = 2$ antisymmetric instability.

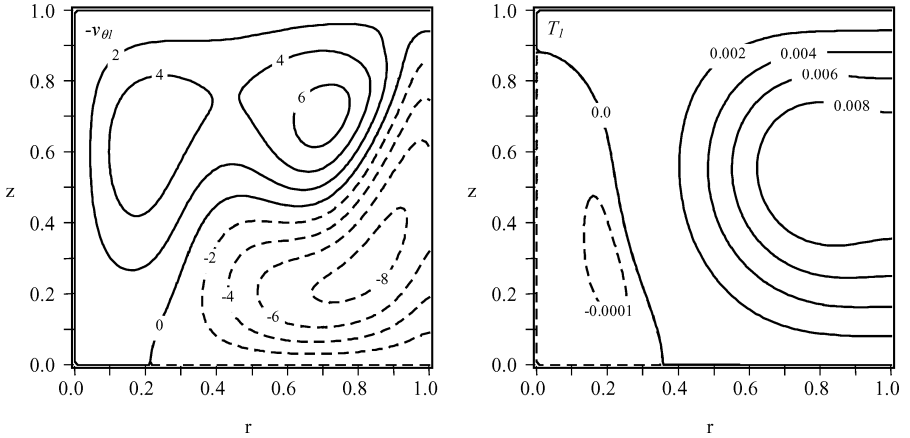

Fig. 5 Perturbation contours of $-v_{\theta 1}$ at $\theta = \pi/4$, and T_1 at $\theta = 0$ for $Pr = 0.02$, $b = 1$, at $Re_{FZ,cr} = 1546$ ($T_{FZ,max} = 1.0007$) for the $m = 2$ antisymmetric instability.

models become more significant. These discrepancies are attributed to the difference in the thermal boundary conditions of the HZ and FZ and the resulting role of convective heat transfer. Discussions are divided into sections concerning the three regions of the FZ analysis, across which the critical disturbance switches from antisymmetric to symmetric and back. First, the antisymmetric mode for $Pr < 0.041$ is discussed. This is followed by a description of the symmetric mode for $0.041 < Pr < 0.079$ and then the antisymmetric mode for $0.079 < Pr \leq 0.2$. Clearly the limits on these ranges would vary with small modifications to the heat flux. However, similar instability mechanisms should be observed for any reasonably similar heat-flux boundary condition. Finally, the energy analysis is explored and compared to the results of Levenstam et al.[7] and Prange et al.[14]

Antisymmetric Instability for $b = 1$, $Pr < 0.041$

The base-flow streamlines and isotherms are given in Fig. 4 for $Pr = 0.02$ at $Re_{FZ,cr} = 1546$. Superimposed on the streamlines is the vector plot of the perturbation components $v_{r1} + v_{z1}$ at $\theta = 0$. Contour plots of T_1 and $-v_{\theta 1}$ are given in Fig. 5. These plots are representative of all of the $Pr < 0.041$ cases. At $\theta = 0$, the center of

the upper toroidal cell is pushed up and inward by the perturbation velocity. The lower cell is pushed up and outward. Therefore, in the $\theta = 0$ plane, the base flow is essentially reinforced for $z > 0$ and opposed for $z < 0$. The perturbation flow feeds a positive $v_{\theta 1}$ into the interior for $z > 0$ and a negative $v_{\theta 1}$ for $z < 0$. At $\theta = \pi/2$, the perturbation velocities oppose the upper toroidal base flow and strengthen the lower. The circulation is completed by means of $v_{\theta 1}$ moving in the negative θ direction along the free surface for $z > 0$ and in the positive direction for $z < 0$. From Fig. 5 we see that the flow along the free surface is driven from a cooler region to a hotter region, just the opposite of what would happen if the instability were driven by thermocapillary effects. Therefore, the instability mechanism, for small *Pr*, can be concluded to be hydrodynamic in nature, in agreement with the HZ.[7] Also, because the temperature differences induced by the perturbation are very small relative to the magnitude of the flow, it would be very difficult to observe this temperature difference experimentally. It should be noted that contours of the perturbation variables look surprisingly similar to those for the HZ at this *Pr*, despite the fact that there is now flow across $z = 0$. The presence of the lower wall in the HZ forces the flow coming toward $z = 0$ to turn along it. As a result, the primary role played by the lower wall in the HZ is probably that of stabilizing the flow by removing momentum through the no-slip condition and the resulting action of viscosity, so that the flow is weaker than in the FZ. This, coupled with the constraint of simply not allowing flow to cross $z = 0$, explains why the critical *Re* is higher for the HZ than the FZ, even though the instability mechanism is not significantly different. Like the HZ, $Re_{\mathrm{FZ,cr}}$ becomes nearly constant at small *Pr*. For both $Pr = 10^{-6}$ and 10^{-10}, $Re_{\mathrm{FZ,cr}} = 1192.7$ ($T_{\mathrm{FZ,max}} = 1.0633$), whereas the limiting value in the HZ is $Re_{\mathrm{HZ,cr}} = 1784$ (Ref. 6).

Symmetric Instability for $b = 1$, $0.041 < Pr < 0.079$

At approximately $Pr = 0.041$, the $m = 2$ steady symmetric mode, which is marginally more stable than the antisymmetric mode for smaller *Pr*, becomes critical. This mode remains critical until $Pr \approx 0.079$. $Re_{\mathrm{FZ,cr}}$ increases rapidly over this range. However, rescaling to $Re_{\mathrm{HZ,cr}}$, as in Fig. 2, shows that, compared to the HZ, the increase is relatively gradual. The base-flow streamlines and isotherms for $Pr = 0.0667$ are given in Fig. 6. The isotherms are clearly altered by convection, which reduces the maximum temperature from 1.0007 (at the critical point for $Pr = 0.02$), to approximately $T_{\mathrm{FZ,max}} = 0.624$. The perturbation velocity vectors at $\theta = 0$ are again superimposed on the streamlines. As shown here, these oppose the base flow in the upper toroidal cell at $\theta = 0$. The lower cell will also be opposed at $\theta = 0$, and both will be reinforced at $\theta = \pi/2$. The disturbance circulation between these two boundaries of the quadrant wedge is completed by azimuthal flow moving in the negative θ direction near the walls ($z = \pm b$) and returning in the positive θ direction at $z = 0$. The temperature perturbation is weak, similar to that for the $Pr = 0.02$ instability. There is no association of T_1 with either $v_{\theta 1}$ or v_{z1} along the free surface. Thus, thermocapillary effects remain unimportant to the instability mechanism. The $m = 3$ oscillatory mechanism, observed by Levenstam et al.[7] in the HZ for $0.057 < Pr \leq 0.0697$, is also hydrodynamic in nature.

For a fixed *Re*, as the *Pr* increases, the maximum temperature of the base flow decreases. This results in a decrease in $\Psi_{\max}$, which is a measure of the strength of the flow. Thus we expect $Re_{\mathrm{FZ,cr}}$ to increase as *Pr* increases, as observed here. The maximum temperature decreases slower than $Re_{\mathrm{FZ,cr}}$ increases, so that $Re_{\mathrm{HZ,cr}} = T_{\mathrm{FZ,max}} Re_{\mathrm{FZ,cr}}$ also increases. The effect of convection is not as dramatic in the half zone, but the lower wall removes enough energy from the flow so that $Re_{\mathrm{HZ,cr}}$ still increases more rapidly with *Pr* than in the full zone.

Antisymmetric Instability for $b = 1$, $0.079 < Pr \leq 0.2$

For $Pr > 0.079$, the nature of the instability changes dramatically as compared to both the lower *Pr* full-zone cases and the half-zone predictions. Unlike the HZ, which becomes unstable to periodic disturbances ($m = 2$ or 3, see Refs. 4, 6, 7), the critical disturbance to the FZ remains steady with $m = 2$. However, the symmetry switches back to the antisymmetric mode. Also, where $Re_{\mathrm{HZ,cr}}$ for the HZ decreases for increasing *Pr*, the FZ is dominated by a nearly constant $Re_{\mathrm{HZ,cr}}$. In this region, $T_{\mathrm{FZ,max}}$ continues to decrease, though less rapidly, as shown in Fig. 3. The result is that $Re_{\mathrm{FZ,cr}}$ continues to increase for $Pr > 0.09$ (after experiencing a minor dip over $0.079 < Pr < 0.09$). This region marks the most significant departure of the two models.

The cause of this discrepancy is apparent from the streamlines and isotherms of Fig. 7 for $Pr = 0.2$ at $Re_{\mathrm{FZ,cr}} \approx 19 \times 10^3$. Because the *Pr* is nearing unity and $Re_{\mathrm{FZ,cr}}$ for transition is very large, thermal convection terms begin to become very important. The upward base flow along the free surface convects with it much of the incoming energy flux. By doing so, it confines most of the axial temperature gradient to the top corner of the melt. However, an axial temperature gradient is required to drive the flow, so that, by reducing the region of strong thermocapillary driving force, the flow weakens itself. The steady axisymmetric base flow then must be a balance of thermocapillary stresses and convection, which fight to intensify and weaken the flow, respectively. Unlike in the HZ, where the temperature at $z = 0$ is fixed to be unity, the convection in the FZ can greatly reduce the temperature at this location. For $Pr = 0.2$, at the critical point, the temperature at $r = 1$, $z = 0$ is reduced to approximately 0.35. Thus the driving potential for the thermocapillary flow is significantly reduced from that of the HZ. This causes the properly scaled critical Reynolds number of the FZ ($Re_{\mathrm{FZ,cr}}$) to continue to increase, whereas in the HZ, the critical Reynolds number ($Re_{\mathrm{HZ,cr}}$) decreases significantly.

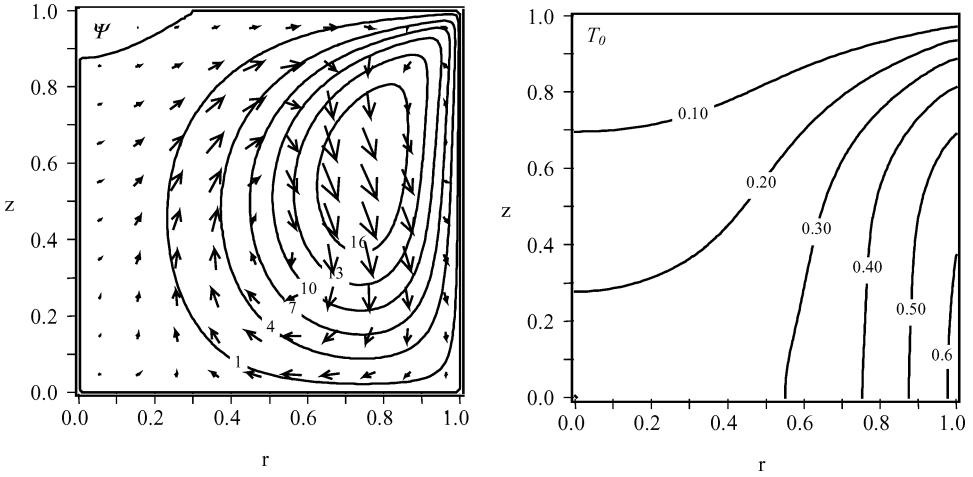

Fig. 6 Base-flow streamlines with perturbation velocity vectors defined by $v_{r1} + v_{z1}$ at $\theta = 0$, and isotherms for $Pr = 0.0667$, $b = 1$ at $Re_{\mathrm{FZ,cr}} = 6505$ ($T_{\mathrm{FZ,max}} = 0.624$) for the $m = 2$ symmetric instability.

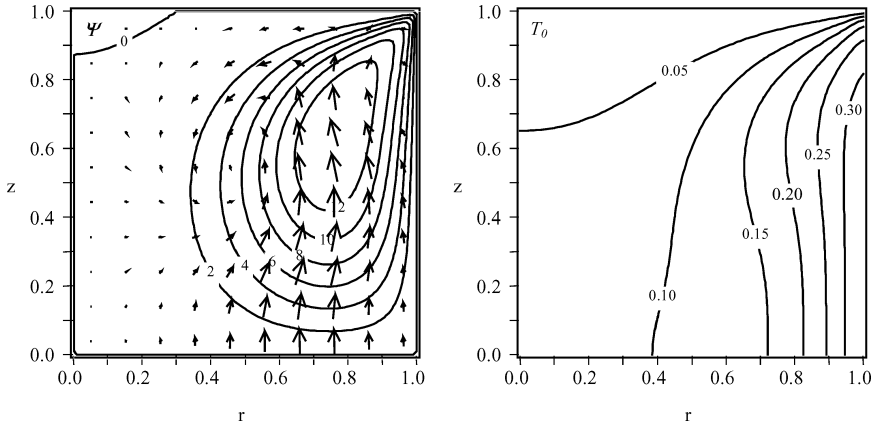

Fig. 7 Base-flow streamlines with perturbation velocity vectors defined by $v_{r1} + v_{z1}$ at $\theta = 0$, and isotherms for $Pr = 0.2$, $b = 1$, at $Re_{FZ,cr} \approx 19 \times 10^3$ ($T_{FZ,max} = 0.351$) for the $m = 2$ antisymmetric instability.

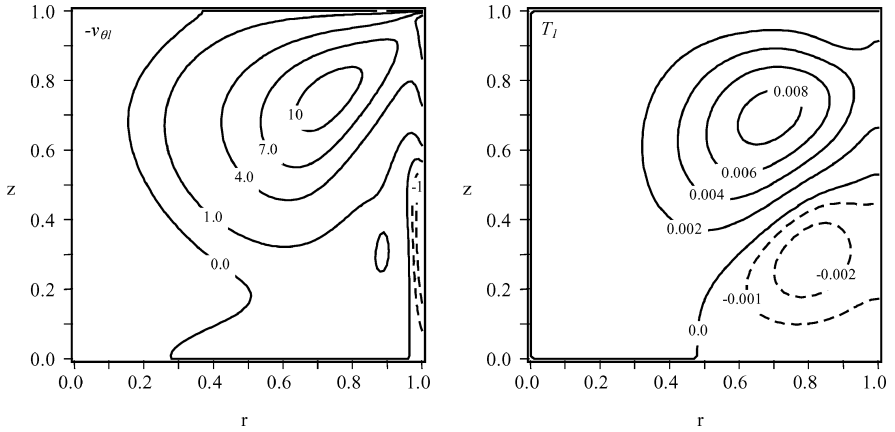

Fig. 8 Perturbation contours of $-v_{\theta 1}$ at $\theta = \pi/4$, and T_1 at $\theta = 0$ for $Pr = 0.2$, $b = 1$, at $Re_{FZ,cr} \approx 19 \times 10^3$ ($T_{FZ,max} = 0.351$) for the $m = 2$ antisymmetric instability.

The disturbance flow is plotted in Fig. 7 (velocity vectors at $\theta = 0$) and Fig. 8. At the boundary of each quadrant, the perturbation flow is dominated by either an upward (as in Fig. 7) or a downward flow through the middle of the base flow toroidal cells. In Fig. 8, the azimuthal velocity and temperature perturbations are plotted at $\theta = \pi/4$ and 0, respectively. The azimuthal flow along the free surface clearly follows the T_1 contours from regions of hot to cold, indicating that the instability mechanism is either driven or reinforced by thermocapillary effects. However, the temperature fluctuations along the free surface are still three to four orders of magnitude smaller than the perturbation velocity. This mode suggests that the transition from a hydrodynamic to a thermocapillary instability mechanism is beginning to arise. A similar transition is observed by Levenstam et al.,[7] in which the thermocapillary and hydrodynamic instabilities compete for dominance over the region $0.0697 < Pr \leq 0.183$, although they observe a periodic mode, more characteristic of a thermocapillary instability than the FZ steady mode.

Transferring Energy to the Disturbance

For $Pr < 0.2$, the most significant terms from the energy analysis appear in the energy form of the axial momentum equation (11b). For Pr less than approximately 0.03, the dominant production term is $-v_{r1} v_{z1} (\partial v_{zo}/\partial r)$, which is positive over nearly the entire flow domain. This term is shown for $Pr = 0.001$, $b = 1$, in Fig. 9. This is consistent with the findings of Prange et al.[14] for $Pr = 0.02$. However, as the Pr increases into the range of antisymmetric modes with $Pr > 0.079$, the term $-v_{z1}^2 (\partial v_{zo}/\partial z)$ from (11b) makes the largest local contribution to the disturbance energy. At this point, $-v_{r1} v_{z1} (\partial v_{zo}/\partial r)$ fails to be a global energy provider. These terms are shown in Fig. 10 for $Pr = 0.1$, $b = 1$. The contribution of $-v_{z1}^2 (\partial v_{zo}/\partial z)$ near the top corner ($r = 1$, $z = b$) increases in significance as the Pr increases. $Re_{FZ,cr}$ increases with Pr, and therefore so does v_{zo} along the free surface, over nearly the entire range of Pr studied (the exception is over the range $0.079 < Pr < 0.1$, where there is a 2–5% decrease in these values). At the top wall, v_{zo} must go to zero, so $\partial v_{zo}/\partial z$ becomes extremely large in magnitude. This corner clearly plays an important role in the transition, as indicated by the fact that $Re_{FZ,cr}$ becomes much more sensitive to the regularization parameter α as the Pr is increased above 0.1. This is discussed in detail in the numerical aspects section.

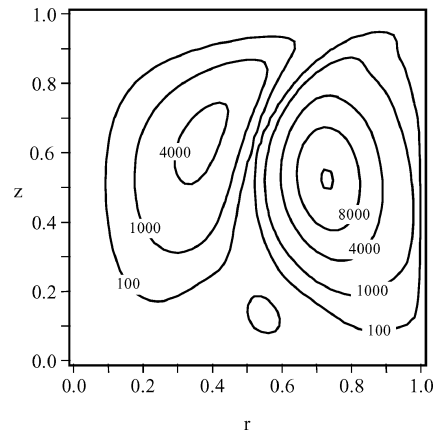

Fig. 9 Contributions to the rate of change of energy in the axial disturbance flow from $-v_{r1} v_{z1} (\partial v_{zo}/\partial r)$ for $Pr = 0.001$, $b = 1$, at $Re_{FZ,cr} = 1205$ ($T_{FZ,max} = 1.0613$) for the $m = 2$ antisymmetric instability.

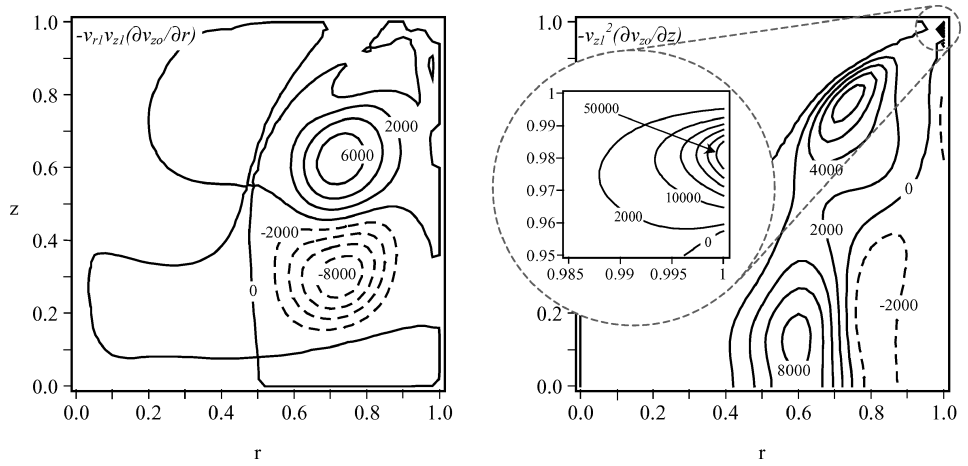

Fig. 10 Contribution to $\frac{1}{2}[\partial(v_{z1}^2)/\partial t]$ from $-v_{r1}v_{z1}(\partial v_{zo}/\partial r)$ and $-v_{z1}^2(\partial v_{zo}/\partial z)$ for $Pr = 0.1$, $b = 1$, at $Re_{FZ,cr} = 11.7 \times 10^3$ ($T_{FZ,max} = 0.479$) for the $m = 2$ antisymmetric instability.

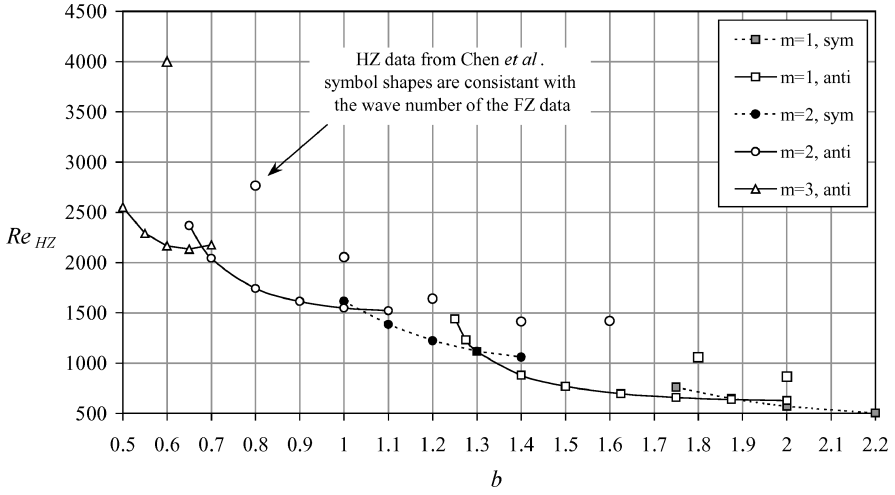

Fig. 11 $Re_{HZ,cr}$ vs b for the FZ with $Pr = 0.02$ and the corresponding HZ data taken from Chen et al.[6] All transitions are to three-dimensional steady flow.

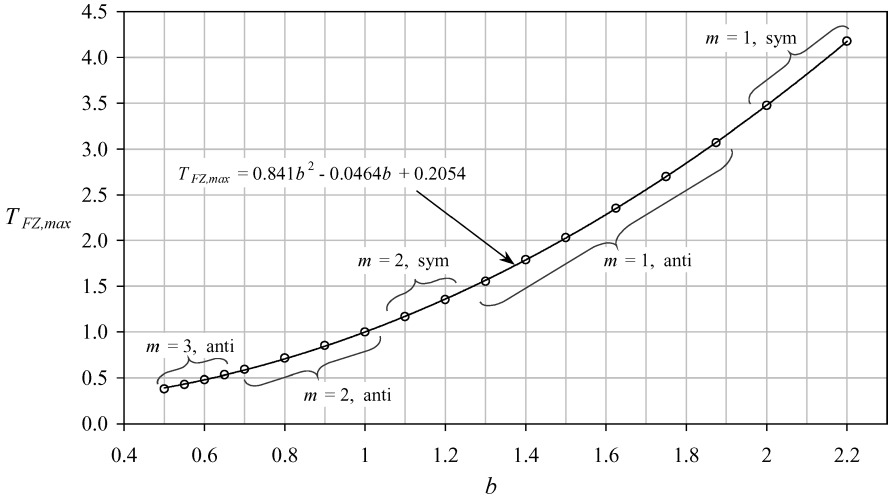

Fig. 12 $T_{FZ,max}$ vs b for the FZ with $Pr = 0.02$, All transitions are to three-dimensional steady flow.

Varying the Aspect Ratio of the Zone

A comparison of the HZ and FZ for $Pr = 0.02$ and $\frac{1}{2} < b < 2$ is given by Figs. 11 and 12. $Re_{HZ,cr}$ is plotted vs b in Fig. 11, with HZ data taken from Chen et al.[6] The maximum dimensionless temperature is plotted vs b for the FZ in Fig. 12. The trends of the two models are consistent. As b decreases, both the critical Re_{HZ} and the critical wave number increase. The mode switching is most easily understood by fixing the height and varying the radius, in which case a small b corresponds to a short zone with large radius. As the radius increases for a fixed height, we expect it to be difficult for instabilities to propagate around the entire free surface. That is, for an $m = 1$ mode, the disturbance circulation would have a very long path in the azimuthal direction as compared to the axial direction. However, if m increases as observed here, the path the disturbance must take is on the same order in all directions.

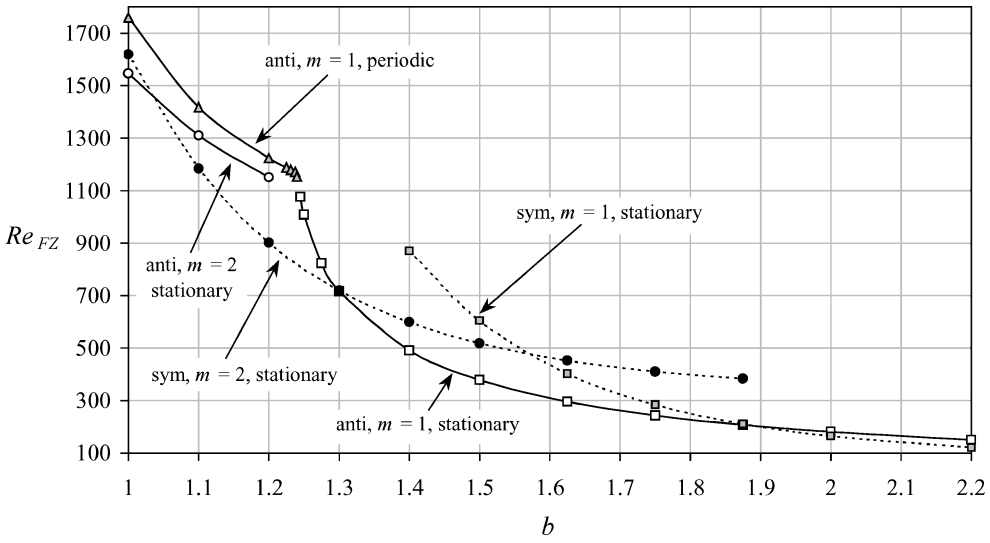

Fig. 13 $Re_{FZ,cr}$ **vs** b **for the FZ with** $Pr = 0.02$**, including the secondary periodic instability for** $m = 1$**.**

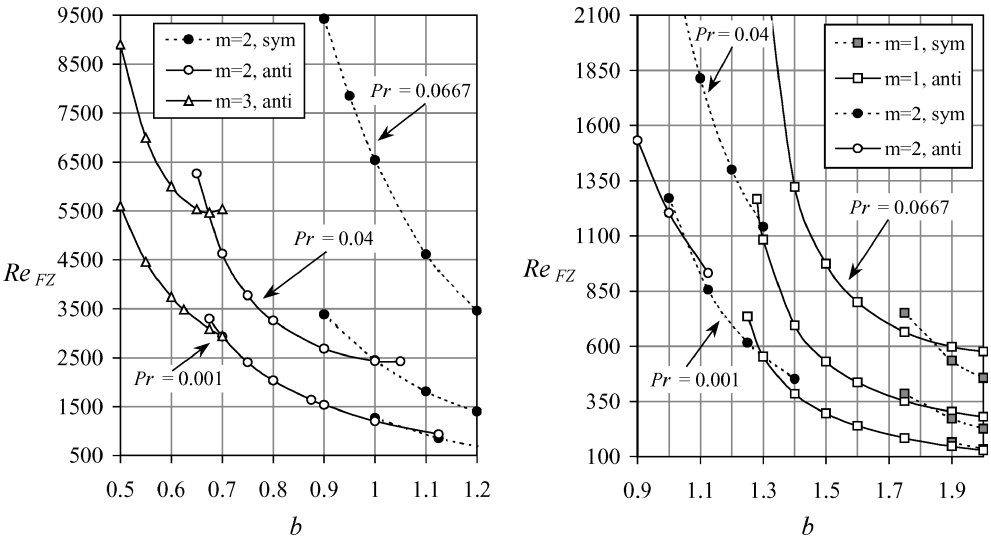

Fig. 14 $Re_{FZ,cr}$ **vs** b **for the FZ for** $Pr = 0.001$**, 0.04, and 0.0667. All transitions are to three-dimensional steady flow.**

$Re_{FZ,cr}$ is plotted for $Pr = 0.02$ in Fig. 13. Here, the supercritical antisymmetric $m = 1$ mode is also traced. It is observed that this mode transitions from a steady to a periodic mode as b is reduced through $b = 1.24$. It appears that the instability transitions smoothly from a steady mode to a periodic mode with very low frequency, and then the frequency increases as b decreases. At $b = 1$, the frequency λ_i has increased from 0 to approximately 20. The linear stability analysis is not formally valid in this region, due to the fact that $m = 2$ symmetric and/or antisymmetric modes have already become unstable. However, it suggests that the frequency of the secondary periodic mode, which is observed experimentally, might be very sensitive to aspect ratios near $b = 1$. As this is the most common aspect ratio used in experiments, this could explain the wide range of frequencies observed by different researchers. The data from this supercritical branch are given in the Appendix.

$Re_{FZ,cr}$ vs b is plotted for $Pr = 0.001$, 0.04, and 0.0667 in Fig. 14. All show the same trends of increases in both $Re_{FZ,cr}$ and m as b is reduced. Though the onset of the primary instability is rarely investigated in experimental studies, the surface-flow visualizations of Takagi et al.[21] in a $Pr = 0.01$ liquid bridge with $b = 2.02$ suggest that the first instability is a steady three-dimensional mode with wave number 1. This is supported by our findings for $b = 2$. As b increases, we eventually expect to see the $b \gg 1$ result given by Xu and Davis,[22] where the instability mechanism involves hydrothermal waves propagating along the free surface. At $b = 2$, the base flow is still highly dependent on the presence of the end walls, and we do not observe hydrothermal waves. The data from Figs. 11–14 are given in the Appendix.

Lappa[11] treated a similar full-zone model for $Pr = 0.01$, using a three-dimensional time integration. However, the flux condition used was based on a radiation balance and therefore deviated slightly from the parabolic flux used here. For $b = 1$, Lappa found a critical Marangoni number that translates to $Re_{FZ,cr} = 1241.3$, for an $m = 2$, antisymmetric disturbance. We found that $Re_{FZ,cr} = 1336.9$, with the same wave number and symmetry. Given the significant difference in the codes, this is a reasonable comparison. However, it would typically be expected that a nonlinear code would predict a higher critical value than a linear stability analysis, as was observed in the HZ by Levenstam et al.[7] Lappa observed mode switching, with increases in m, as b was reduced. The mode switches are, however, "faster" than those predicted by our code. That is, the jumps occur over shorter ranges of b, go to larger values of m, and are not all unit increases. In the three-dimensional code, these jumps can be explained as the result of nonlinear interactions between two modes, which then favor a new mode with higher azimuthal wave number, at slightly supercritical Re. The same logic could explain why only

antisymmetric modes are observed by Lappa, whereas we observe both symmetries, as b is varied. In Fig. 14, for $Pr = 0.001$, antisymmetric modes are present at values of Re_{FZ} slightly larger than the critical values for the symmetric modes. It is completely reasonable to expect a three-dimensional code to prefer the secondary mode, particularly if it has a higher growth rate than the primary mode. Such an affinity for supercritical modes was also observed by Levenstam et al.[7] for the $m = 3$ and 4 oscillatory modes in their three-dimensional studies of the HZ.

Numerical Aspects

A representative sample of the numerical accuracy of the results is discussed below. Two measures were taken in developing the code to ensure high accuracy while maintaining reasonable computational costs. First, splitting the domain in half, and treating the antisymmetric and symmetric modes separately, was essential to achieving sufficient resolution. If the full domain is treated, twice as many grid points are needed. Furthermore, half of the coefficients in the perturbation variables would be zero, because the inherent symmetry would still exist. Therefore, treating only $0 \le z \le b$ is doubly advantageous. Second, we have found that applying the expansions of the governing equations, particularly at $r = 0$, allows us to maintain smooth base flows to very high Re, with almost no additional computational costs. We do not waste resolution by rescaling the grid to place many points near $r = 0$, nor do we have to live with a large gap between $r = 0$ and the first collocation point. The cost of this method is, of course, the time and effort it takes to derive and code the equations, but the reward of numerical accuracy is more than adequate justification.

Grid- and α-Dependence Studies

Grid dependence studies representative of those performed for all Pr for $b = 1$ are given in Table 1. Many digits are listed only to show that there were in fact quantifiable differences in the predicted values of $Re_{FZ,cr}$ for different base-flow grids. The base-flow grids are listed in the order NRF × NZF, NRT × NZT as described in the base-flow section of the problem formulation. The accuracy of the calculations do not extend to this many significant digits, but clearly grid resolution was achieved for all Pr. This is attributed to the measures highlighted earlier.

Table 1 Grid-dependence studies based on $Re_{FZ,cr}$ for select cases over a range of Pr with $b = 1$

	Stability analysis grid	
Base flow grid	28×28	30×42
$Pr = 0.001$ with $\alpha = 300$		
25×35, 10×10	1204.9436	1204.9436
30×40, 20×20	1204.9439	1204.9439
$Pr = 0.02$ with $\alpha = 300$		
25×40, 10×10	1546.575	1546.575
30×50, 15×15	1546.581	1546.581
	30×42	32×52
$Pr = 0.0667$ with $\alpha = 500$		
30×40, 20×20	6522.83	6522.75
35×55, 25×25	6522.76	6522.74
	30×50	32×60
$Pr = 0.2$ with $\alpha = 1300$		
30×50, 25×25	18776.3	18776.7
35×65, 30×30	18776.5	18777.2

However, achieving independence from the regularization parameter α was more difficult. This is illustrated by Table 2 for cases with $b = 1$. The regularization parameter smoothes out the boundary condition inconsistencies that arise from enforcing that $r = 1$, $z = b$ is a sharp corner. To do so, it reduces the gradient of the free-surface temperature in this corner, which amounts to reducing the driving term of the flow. Therefore, as α is increased, this damping effect decreases, and we expect $Re_{FZ,cr}$ to decrease also. If α can be increased to the point at which further increases do not affect the value of $Re_{FZ,cr}$, it can then be concluded that it no longer plays a significant role in the instability mechanism, but still allows the numerical solution to be smooth enough to be well behaved.

For $Pr = 0.001$ and 0.02, and $b = 1$, $Re_{FZ,cr}$ drops predictably and rapidly with increases in α, to within the accuracy of the calculations by $\alpha = 400$. This was true for all $b = 1$ cases with $Pr \le 0.04$. By $Pr = 0.06$, it was necessary to increase α to 800 to maintain, at most, a 0.25% difference in $Re_{FZ,cr}$ between the largest consecutive values of α. This required increase in α is demonstrated by the values of $Re_{FZ,cr}$ for $Pr = 0.0667$ and 0.075 in Table 2.

As the Pr is increased further, the problem is greatly magnified due to the concentration of the temperature gradient and $\partial v_{zo}/\partial z$ in the top corner, coupled with the continued increase in $Re_{FZ,cr}$. This is shown clearly by the packing of the isotherms and streamlines in Fig. 7 for $Pr = 0.2$, $b = 1$, at $Re_{FZ,cr} \approx 19 \times 10^3$. Most of the free surface is nearly isothermal, and therefore does not contribute to the driving thermocapillary boundary condition. The only significant gradient occurs at the same location where the regularization is most harmful. The thermocapillary boundary condition is applied on the Ψ grid. Therefore, to resolve the boundary condition, the number of axial points needed in the Ψ grid increases rapidly with Pr. Also, the temperature grid must be significantly finer than in the lower Pr cases, in order to capture the axial-temperature gradient in the corner.

Grid and regularization parameter studies for aspect ratios of 1 show that the values of $Re_{FZ,cr}$ presented here are converged within 0.1% for $Pr \le 0.02$, and within 1% for $Pr \le 0.08$. For $0.08 < Pr \le 0.2$, the nature of free surface-temperature distribution makes it increasingly difficult to achieve regularization parameter independence. This is most readily identified by the fact that $Re_{FZ,cr}$ begins increasing with increases in α, for the antisymmetric modes with $Pr > 0.09$, as shown in Table 2. Despite the fact that these flows remain grid-independent, and show no sign of breakdown in resolution, we must conclude that the regularization, as applied here, is no longer appropriate due to the importance of resolving the gradients in the top corner. As a consequence, the values of $Re_{FZ,cr}$ in this range are converged only to within ~4%. However, because both the base-flow isotherms and the instability mechanisms in the full zone are very different from those predicted by the half-zone model for $Pr > 0.079$, the numerical error was overlooked for the present in favor of discussing the physics of these flows. Treating the full zone accurately at larger Pr with our fully numerical scheme does not appear to be feasible. This is most likely an indication that this is not an appropriate model of floating-zone crystal growth for order-one Pr, where the top boundary would certainly not be flat,

Table 2 Regularization parameter influence on $Re_{FZ,cr}$ for a range of Pr with $b = 1$

Pr	$Re_{FZ,cr}$ for				% difference in predicted $Re_{FZ,cr}$ for		
	$\alpha = 100$	*$\alpha = 200$*	*$\alpha = 300$*	*$\alpha = 400$*	*$\alpha = 100$ and 400*	*$\alpha = 200$ and 400*	*$\alpha = 300$ and 400*
0.001	1,207.2	1,205.3	1,204.9	1,204.8	0.199%	0.0415%	0.00830%
0.02	1,552.1	1,547.6	1,546.6	1,546.2	0.382%	0.0905%	0.0259%
	$\alpha = 200$	*$\alpha = 300$*	*$\alpha = 500$*	*$\alpha = 800$*	*$\alpha = 200$ and 800*	*$\alpha = 300$ and 800*	*$\alpha = 500$ and 800*
0.0667	6,645	6,569	6,523	6,505	2.15%	0.984%	0.277%
0.075	9,998	9,945	9,805	9,749	2.55%	2.01%	0.574%
	$\alpha = 800$	*$\alpha = 1300$*	*$\alpha = 5000$*	*$\alpha = 8000$*	*$\alpha = 800$ and 8000*	*$\alpha = 1300$ and 8000*	*$\alpha = 5000$ and 8000*
0.1	11,611	11,643	11,689	11,695	0.718%	0.445%	0.0513%
0.2	18,624	18,777	19,020	19,056	2.27%	1.46%	0.189%

Table 3 Regularization parameter influence on $Re_{FZ,cr}$ for a range of b with $Pr = 0.02$ and 0.04

	$Re_{FZ,cr}$ for				% difference in predicted $Re_{FZ,cr}$ for		
	$\alpha = 100$	$\alpha = 200$	$\alpha = 300$	$\alpha = 400$	$\alpha = 100$ and 400	$\alpha = 200$ and 400	$\alpha = 300$ and 400
$Pr = 0.02$, b:							
0.50	6672	6688	6695	6698	0.388%	0.149%	0.0448%
0.75	2841	2844	2845	2846	0.176%	0.0703%	0.0351%
1.5	377.89	378.08	378.23	378.32	0.114%	0.0634%	0.0238%
2.0	164.956	164.795	164.784	164.788	0.102%	0.00425%	0.00243%
$Pr = 0.04$, b:							
0.50	8840	8879	8893	8900	0.674%	0.236%	0.0787%
0.75	3762	3768	3772	3774	0.318%	0.159%	0.0530%
1.5	529.47	529.74	530.09	530.31	0.158%	0.107%	0.0415%
2.0	281.57	280.84	280.83	280.88	0.246%	0.0142%	0.0178%

and the true flux condition would probably deviate greatly from parabolic.

When the aspect ratio was varied the grid convergence was rapid, and the results were, again, more sensitive to the regularization parameter. A sample of the regularization parameter-dependence studies performed for a fixed Pr and varying b are given in Table 3. In general, a larger α and more grid points were required as b was varied up or down from 1. As b increases, the height of the zone increases and therefore more grid points are required in the axial direction. However, because $Re_{FZ,cr}$ decreases as b increases, the influence on grid requirements and regularization parameter is marginal. As b decreases, $Re_{FZ,cr}$ increases rapidly, and a much finer grid is required. The results also become much more sensitive to α as b approaches 0.5.

Conclusions

Replacing the $z = 0$ plane in the FZ with a wall to create the HZ model significantly alters the stability of the flow. The presence of the lower wall in the HZ stabilizes the flow by removing momentum through the no-slip condition and confining the flow by way of the no-penetration condition. Therefore, the stability analysis of the HZ overestimates the adjusted $Re_{HZ,cr}$ of the FZ.

However, the instability mechanisms for both models are hydrodynamic in nature and are somewhat stabilized by secondary thermocapillary effects for very small Pr ($Pr < 0.079$ for the FZ with $b = 1$). At larger Pr, both models have a range where the instability mechanisms are aided by thermocapillary phenomena, though they remain primarily hydrodynamic in nature. As the Pr is further increased, the HZ becomes susceptible to a purely thermocapillary instability. This mechanism has not been observed in the FZ because the progression through the mechanisms as Pr is varied is slower than in the HZ. This is attributed to the differences in the thermal boundary conditions. In the HZ, the walls are always maintained at constant temperature, so that the temperature difference between the walls is of order one. In the FZ, convection drops the temperature difference significantly as the Pr is increased. This reduces the thermocapillary driving strength, and a balance is achieved. To observe the oscillatory instability in a full-zone model at order-one Pr, it may be necessary to provide more realistic boundary conditions, particularly the shape of the top boundary.

As b decreases, both models are characterized by increases in both $Re_{HZ,cr}$ and m_{cr}. The increase in $Re_{HZ,cr}$ is explained by the increase in the ratio of wall surface area to melt volume as b decreases. The critical wave number increases so that the path the disturbance takes around the free surface is comparable in length to the path of the disturbance in the r–z plane.

It is likely that the stationary modes, for small Pr typical of semiconductor melts, have not often been observed experimentally because the temperature fluctuations on the free surface are very weak. The presence of periodic instabilities at marginally supercritical Re suggests that the modes that are typically observed in floating-zone crystal growth do exist in the FZ model and could possibly be investigated with a weakly nonlinear analysis.

We have shown that the exhaustive study of the HZ has set an excellent foundation for our understanding of the floating-zone crystal growth method. Furthermore, there is clearly a need to move toward more realistic models, as shown both by our work, and by the work of many other researchers. With the numerical analysis and model improvements presented here, we hope to have aided in bringing the community closer to a full understanding of this promising crystal growth method.

Appendix: Critical Curve Data

Table A1 contains the data used to generate Figs. 2 and 3, for $b = 1$. Table A2 lists the data from Figs. 11, 12, and 13 for $Pr = 0.02$. Table A3 contains the data about the supercritical, $m = 1$ mode shown in Fig. 13. Tables A4 and A5 list the data used to plot Fig. 14.

Table A1 $Re_{HZ,cr}$, $T_{FZ,max}$, and the axial disturbance symmetry vs Pr for $b = 1$, $m_{cr} = 2$, for the FZ

Pr	$Re_{HZ,cr}$	$T_{FZ,max}$	Symmetry
10^{-10}	1268.179	1.063307	anti
10^{-6}	1268.189	1.063305	anti
0.001	1278.85	1.0613	anti
0.01	1388.3	1.0384	anti
0.015	1461.9	1.0213	anti
0.02	1547.3	1.0007	anti
0.025	1649	0.976	anti
0.03	1772	0.948	anti
0.035	1926	0.915	anti
0.04	2129	0.876	anti
0.041	2179	0.867	anti
0.041	2182	0.867	sym
0.044	2306	0.842	sym
0.045	2353	0.834	sym
0.05	2608	0.790	sym
0.055	2930	0.742	sym
0.06	3335	0.693	sym
0.063	3631	0.662	sym
0.0667	4059	0.624	sym
0.068	4227	0.611	sym
0.07	4504	0.591	sym
0.075	5292	0.543	sym
0.079	6003	0.508	sym
0.079	5949	0.510	anti
0.08	5909	0.509	anti
0.09	5677	0.495	anti
0.1	5606	0.479	anti
0.11	5608	0.463	anti
0.13	5727	0.433	anti
0.15	5937	0.406	anti
0.175	6281	0.377	anti
0.2	6696	0.351	anti

Table A2 $Re_{FZ,cr}$, $T_{FZ,max}$, m_{cr}, and the axial disturbance symmetry vs b for $Pr = 0.02$

b	$Re_{HZ,cr}$	$T_{FZ,max}$	m_{cr}	Symmetry
0.50	6697.5	0.3811	3	anti
0.55	5321.5	0.4302	3	anti
0.60	4500.6	0.4814	3	anti
0.65	3992.8	0.5345	3	anti
0.70	3456.3	0.5911	2	anti
0.80	2431.9	0.7165	2	anti
0.90	1892.2	0.8528	2	anti
1.00	1546.2	1.0007	2	anti
1.10	1183.9	1.1685	2	sym
1.20	901.63	1.3546	2	sym
1.30	719.33	1.5551	2	sym
1.30	716.46	1.5555	1	anti
1.40	490.79	1.7897	1	anti
1.50	378.32	2.0322	1	anti
1.625	295.53	2.3540	1	anti
1.75	243.30	2.6997	1	anti
1.875	207.35	3.0694	1	anti
1.875	211.09	3.0673	1	sym
2.00	164.79	3.4756	1	sym
2.20	120.55	4.1777	1	sym

Table A3 $Re_{FZ,cr}$, λ_i, and the transition mechanism vs b for the supercritical, $m = 1$, antisymmetric instability for $Pr = 0.02$

b	$Re_{FZ,cr}$	λ_i	Mechanism
1.00	1758.6	19.7	periodic
1.10	1416.8	15.3	periodic
1.20	1223.4	8.49	periodic
1.225	1187.8	5.36	periodic
1.23125	1178.4	4.22	periodic
1.2375	1171.4	2.57	periodic
1.24	1153.2	1.68	periodic
1.245	1076.2	0	steady
1.25	1008.1	0	steady
1.275	823.6	0	steady

Table A4 $Re_{FZ,cr}$, m_{cr}, and the axial disturbance symmetry vs b for $Pr = 0.001$ and 0.04 for the FZ

b	$Re_{FZ,cr}$ for $Pr = 0.001$	$Re_{FZ,cr}$ for $Pr = 0.04$	m_{cr}	Symmetry
0.50	5596.9	8900.2	3	anti
0.55	4462.8	7000.0	3	anti
0.60	3747.2	6006.5	3	anti
0.625	3485.8	——	3	anti
0.65	——	5536.4	3	anti
0.675	3091.0	5466.8	3	anti
0.70	2943.0	5536.6	3	anti
0.70	2935.7	4626.1	2	anti
0.75	2407.3	3774.4	2	anti
0.80	2035.0	3259.5	2	anti
0.875	1637.6	——	2	anti
0.90	1532.9	2684.5	2	anti
1.00	1204.8	2432.1	2	anti
1.00	1271.0	2451.8	2	sym
1.10	——	1813.5	2	sym
1.125	855.64	——	2	sym
1.20	——	1400.0	2	sym
1.25	615.27	——	2	sym
1.30	552.85	1083.0	1	anti
1.40	384.96	694.26	1	anti
1.50	295.81	530.30	1	anti
1.60	238.94	435.99	1	anti
1.75	183.50	352.17	1	anti
1.90	147.12	302.90	1	anti
2.00	129.07	280.88	1	anti
1.90	165.43	272.79	1	sym
2.00	135.28	226.37	1	sym

Table A5 $Re_{FZ,cr}$, m_{cr}, and the axial disturbance symmetry vs b for $Pr = 0.0667$, for the FZ

b	$Re_{FZ,cr}$ for $Pr = 0.0667$	m_{cr}	Symmetry
0.90	9425	2	sym
0.95	7850	2	sym
1.00	6505	2	sym
1.10	4612	2	sym
1.20	3459	2	sym
1.30	2816	2	sym
1.275	3078	1	anti
1.30	2388	1	anti
1.40	1323	1	anti
1.50	973.4	1	anti
1.60	799.5	1	anti
1.75	663.7	1	anti
1.90	597.7	1	anti
2.00	575.5	1	anti
1.75	751.2	1	sym
1.90	535.7	1	sym
2.00	456.8	1	sym

Acknowledgments

This work was supported by the National Science Foundation under Grant CTS0346302 and by the National Computational Sciences Alliance under Grant CTS020008N utilized on the Origin2000 Array.

References

[1]Eyer, A., Nitsche, R., and Zimmermann, H., "A Double-Ellipsoid Mirror Furnace for Zone Crystallization Experiments in Spacelab," *Journal of Crystal Growth*, Vol. 47, No. 2, 1979, pp. 219–229.

[2]Bohm, J., Lüdge, A., and Schröder, W., "Crystal Growth by Floating Zone Melting," *Handbook of Crystal Growth, Vol. 2a: Bulk Crystal Growth, Basic Techniques*, edited by D. T. J. Hurle, Elsevier, New York, 1994, pp. 215–257.

[3]Eyer, A., and Leiste, H., "Striation-Free Silicon Crystals by Floating-Zone with Surface-Coated Melt," *Journal of Crystal Growth*, Vol. 71, No. 1, 1985, pp. 249–252.

[4]Wanschura, M., Shevtsova, V. M., Kuhlmann, H. C., and Rath, H. J., "Convective Instability Mechanisms in Thermocapillary Liquid Bridges," *Physics of Fluids*, Vol. 7, No. 5, 1995, pp. 912–925.

[5]Houchens, B. C., and Walker, J. S., "Magnetic Damping of the Thermocapillary Instability During Floating-Zone Crystal Growth in Space," AIAA Paper 2001-5053, Oct. 2001.

[6]Chen, G., Lizée, A., and Roux, B., "Bifurcation Analysis of the Thermocapillary Convection in Cylindrical Liquid Bridges," *Journal of Crystal Growth*, Vol. 180, Nos. 3, 4, 1997, pp. 638–647.

[7]Levenstam, M., Amberg, G., and Winkler, C., "Instabilities of Thermocapillary Convection in a Half-Zone at Intermediate Prandtl Numbers," *Physics of Fluids*, Vol. 13, No. 4, 2001, pp. 807–816.

[8]Sim, B.-C., and Zebib, A., "Thermocapillary Convection in Liquid Bridges with Undeformable Curved Surfaces," *Journal of Thermophysics and Heat Transfer*, Vol. 16, No. 4, 2002, pp. 553–561.

[9]Kasperski, G., Batoul, A., and Labrosse, G., "Up to the Unsteadiness of Axisymmetric Thermocapillary Flows in a Laterally Heated Liquid Bridge," *Physics of Fluids*, Vol. 12, No. 1, 2000, pp. 103–119.

[10]Morthland, T. E., and Walker, J. S., "Magnetic Damping of Axisymmetric Thermocapillary Convection in Float Zones in Microgravity," *Journal of Thermophysics and Heat Transfer*, Vol. 11, No. 4, 1997, pp. 588–590.

[11]Lappa, M., "Three-Dimensional Numerical Simulation of Marangoni Flow Instabilities in Floating Zones Laterally Heated by an Equatorial Ring," *Physics of Fluids*, Vol. 15, No. 3, 2003, pp. 776–789.

[12]Morthland, T. E., and Walker, J. S., "Thermocapillary Convection During Floating-Zone Silicon Growth with a Uniform or Non-Uniform Magnetic Field," *Journal of Crystal Growth*, Vol. 158, No. 4, 1996, pp. 471–479.

[13]Nienhüser, C., and Kuhlmann, H. C., "Stability of Thermocapillary Flows in Non-Cylindrical Liquid Bridges," *Journal of Fluid Mechanics*, Vol. 458, 2002, pp. 35–73.

[14]Prange, M., Wanschura, M., Kuhlmann, H. C., and Rath, H. J., "Linear Stability of Thermocapillary Convection in Cylindrical Liquid Bridges Under Axial Magnetic Fields," *Journal of Fluid Mechanics*, Vol. 394, 1999, pp. 281–302.

[15]Jordan, A. S., "Estimated Thermal Diffusivity, Prandtl Number, and Grashof Number of Molten GaAs, InP and GaSb," *Journal of Crystal Growth*, Vol. 71, No. 3, 1985, pp. 551–558.

[16]Anderson, E., Bai, Z., Bischof, C., Blackford, S., Demmel, J., Dongarra, J., Du Croz, J., Greenbaum, A., Hammarling, S., McKenney, A., and Sorensen, D., *LAPACK User's Guide*, 3rd ed., Society for Industrial and Applied Mathematics, Philadelphia, 1999.

[17]Walker, J. S., Martin-Witkowski, L., and Houchens, B. C., "Effects of a Rotating Magnetic Field on the Thermocapillary Instability in the Floating Zone Process," *Journal of Crystal Growth*, Vol. 252, Nos. 1–3, 2003, pp. 413–423.

[18]Grants, I., and Gerbeth, G., "Stability of Axially Symmetric Flow Driven by a Rotating Magnetic Field in a Cylindrical Cavity," *Journal of Fluid Mechanics*, Vol. 431, 2001, pp. 407–426.

[19]Smith, B. T., Boyle, J. M., Dongarra, J. J., Garbow, B. S., Ikebe, Y., Klema, V. C., and Moler, C. B., *Matrix Eigensystem Routines: EISPACK Guide*, 2nd ed., Springer-Verlag, New York, 1976.

[20]Saad, Y., *Numerical Methods for Large Eigenvalue Problems*, Series in Algorithms and Architectures for Advanced Scientific Computing, Manchester Univ. Press, Manchester, England, U.K., 1992, Chap. IV.

[21]Takagi, K., Otaka, M., Natsui, H., Arai, T., Yoda, S., Yuan, Z., Mukai, K., Yasuhiro, S., Imaishi, N., "Experimental Study on the Transition to Oscillatory Thermocapillary Flow in a Low Prandtl Number Liquid Bridge," *Journal of Crystal Growth*, Vol. 233, Nos. 1, 2, 2001, pp. 399–407.

[22]Xu, J.-J., Davis, S. H., "Convective Thermocapillary Instabilities in Liquid Bridges," *Physics of Fluids*, Vol. 27, No. 5, 1984, pp. 1102–1107.